

Diffractive imaging at large Fresnel number: Challenge of dynamic mesoscale imaging with hard x rays

John L. Barber,^{*} Cris W. Barnes,[†] Richard L. Sandberg,[‡] and Richard L. Sheffield[§]

Los Alamos National Laboratory, Los Alamos, New Mexico 87545, USA

(Received 27 February 2013; revised manuscript received 17 April 2014; published 12 May 2014)

Real materials have structure at both the atomic or crystalline scale as well as at interfaces and defects at the larger scale of grains. There is a need for the study of materials at the “mesoscale,” the scale at which subgranular physical processes and intergranular organization couple to determine microstructure, crucially impacting constitutive response at the engineering macroscale. Diffractive imaging using photons that can penetrate multiple grains of material would be a transformative technique for the study of the performance of materials in dynamic extremes. Thicker samples imply higher energy photons of shorter wavelength, and imaging of multiple grains implies bigger spot sizes. Such imaging requires the use of future planned and proposed hard x-ray free electron lasers (such as the European XFEL) to provide both the spatial coherence transverse to the large spots and the peak brilliance to provide the short illumination times. The result is that the Fresnel number of the system becomes large and is no longer in the Fraunhofer far-field limit. The interrelated issues of diffractive imaging at large Fresnel number are analyzed, including proof that diffractive imaging is possible in this limit and estimates of the signal-to-noise possible. In addition, derivation of the heating rates for brilliant pulses of x rays are presented. The potential and limitations on multiple dynamic images are derived. This paper will present a study of x-ray interactions with materials in this new regime of spatially coherent but relatively large mesoscale spots at very hard energies. It should provide the theory and design background for the experiments and facilities required to control materials in extreme environments, in particular for the next generation of very-hard-x-ray free electron lasers.

DOI: 10.1103/PhysRevB.89.184105

PACS number(s): 42.25.Fx, 42.30.Rx, 61.05.C-, 87.64.Bx

I. THE CHALLENGE OF TRANSIENTLY IMAGING RARE DEFECTS IN LARGE SAMPLES

The grand challenge of materials science is a transformation from the current era of observation to an era of control of the properties of materials [1]. Material properties are often controlled not only by the atomic structure of the material but by the interfaces, inhomogeneities, and defects of the bulk material. Thus the ability to image interfaces or sparse defects in multigranular material as they are dynamically created and evolved *in situ* in extreme environments is critical to the control of materials for many national needs [2]. This is the challenge of mesoscale [3] imaging.

A revolution is occurring in the field of x-ray imaging [4,5]. It has been demonstrated that using extreme ultraviolet or x-ray photons from a spatially coherent source (e.g., an x-ray free electron laser (XFEL) [6])—or a source which can be filtered to coherency (e.g., a spatially filtered synchrotron beamline)—the phase information absent in diffraction pattern intensity data can be retrieved via an iterative algorithm to recover a reconstructed image of the sample. This method was theoretically proposed for two-dimensional samples in 1952 [7] and first achieved experimentally in 1999 [8]. It is now in routine use for a variety of samples including nanocrystals [9,10], viruses [11,12], single cells [13,14], biomolecules [15], and integrated circuits [16] at a variety of

sources of spatially coherent—and partially coherent [17]—light.

In the context of materials science on metals or alloys, by the term “mesoscale” we refer to imaging sample regions containing a few to several grains in linear extent, tens to hundreds of microns in size. Such scales include the morphology of grains and grain boundaries, as well as some smaller-scale intragrain effects. Harder energy photons (x rays) are required to penetrate such a sample. The dual requirements of large spot size and short wavelength result in experiments that are difficult to perform in the Fraunhofer, or far-field, limit where coherent diffraction imaging has traditionally been performed. We begin with a derivation of diffraction theory generalized to the Fresnel—as opposed to the Fraunhofer—regime. We consider the impact of this theory on coherent x-ray diffraction imaging and phase retrieval algorithms. Analysis follows of optimum photon energy, both in terms of maximizing the coherently scattered signal and reducing heating of the sample by the illumination pulse to allow for multiple dynamic images. Finally, example point designs for possible experiments are presented.

II. DIFFRACTION THEORY GENERALIZED TO THE FRESNEL REGIME

In this section, we provide an overview of classical diffraction theory and derive an extension of that theory to the Fresnel regime necessary for mesoscale imaging (large diameter spot sizes with very hard and penetrating x rays). (As explained below, we define the Fresnel regime here as a limitation to diffraction due to the placement of a large sample close to the detector plane, as opposed to Fresnel illumination caused by

^{*}jlbarber@lanl.gov

[†]cbarnes@lanl.gov

[‡]sandberg@lanl.gov

[§]sheff@lanl.gov

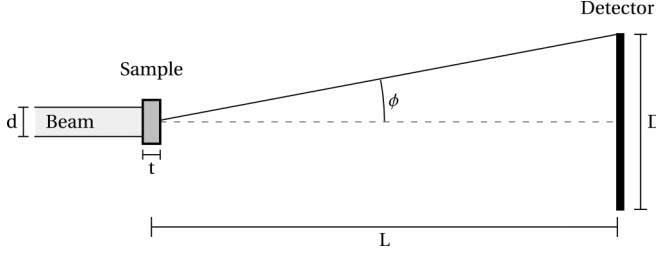


FIG. 1. A schematic x-ray scattering experiment.

a diverging wavefront, such as in Williams *et al.* [18].) We begin by defining the relevant variables that characterize an idealized x-ray scattering experiment, a schematic of which is shown in Fig. 1. (See Appendix for a list of the symbols used in this article.) A beam of coherent, monochromatic light with wavelength λ and photon energy $E_\gamma = hc/\lambda$ (h , Planck's constant; c , the speed of light) is incident upon a sample. As is traditional in x-ray scattering, it is assumed that the beam initially travels in the z direction, with wave vector \vec{k}_i and wave number $k = |\vec{k}_i|$. For an idealized beam with uniform intensity within a circular cross section, the spot size d is that circle's diameter. For more realistic beam profiles, we define d as the full width at half maximum (FWHM) of the radial intensity distribution. The sample's thickness t in the beam direction may be larger or smaller than d . The detector is assumed to be centered along the positive z axis a distance L from the sample, to have a width and height of D , and to consist of N_p^2 square pixels of width and height p , where $N_p = D/p$ is the linear number of pixels in either direction on the detector. Typically, N_p falls in the range $\sim 10^3\text{--}10^4$. The scattering angle subtended by the detector is $\phi = \tan^{-1}(D/2L)$. Note that ϕ is the quantity usually referred to in the scattering literature as $2\theta_{\max}$.

Our goal is to calculate the scattered intensity at a point \vec{r} on the surface of the detector for the experimental setup in Fig. 1. Consider an isolated electron located at a position $\vec{r}' = (x', y', z')$ in three-dimensional space (see Fig. 2). If the electron is bombarded by a beam in the form of an infinite, coherent plane wave with electric field

$$\vec{E}_0(\vec{r}') = E_0 e^{i\vec{k}_i \cdot \vec{r}' \hat{\varepsilon}}, \quad (1)$$

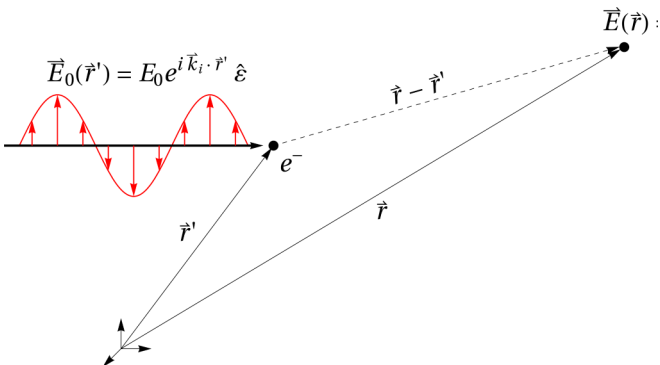


FIG. 2. (Color online) A classical view of an elastic electron/photon scattering event.

where E_0 is the incident electric field amplitude, \vec{k}_i is its wave vector, and $\hat{\varepsilon}$ is its polarization vector, then the resulting oscillation of the electron will yield a scattered radiation field. Via consideration of the corresponding Liénard-Wiechart potentials, it can be shown [19,20] that in the nonrelativistic limit the scattered electric field vector at a point $\vec{r} = (x, y, z)$ is

$$\vec{E}(\vec{r}) = r_e E_0 [(\hat{n} \cdot \hat{\varepsilon}) \hat{n} - \hat{\varepsilon}] \frac{e^{i(k|\vec{r}-\vec{r}'| + \vec{k}_i \cdot \vec{r}')}}{|\vec{r} - \vec{r}'|}. \quad (2)$$

Here $r_e = e^2/mc^2 \sim 2.82 \times 10^{-15}$ m is the classical radius of the electron, and

$$\hat{n} = \frac{\vec{r} - \vec{r}'}{|\vec{r} - \vec{r}'|} \quad (3)$$

is a unit vector from the source point \vec{r}' to the field point \vec{r} . Note that a number of approximations have been made in arriving at the expression in Eq. (2). In particular, we have assumed that the beam is perfectly coherent, monochromatic, planar, and infinite in extent, an ideal which is not achievable in practice (see Sec. V for further discussion of the coherence issue). Furthermore, we have considered only classical elastic scattering, and ignored inelastic (Compton) scattering, which is quantum mechanical in origin. The latter is justified by the fact that Compton scattering becomes significant only when E_γ approaches the electron rest energy 511 keV.

If, instead of a single isolated electron, the beam is incident upon a sample with an extended electron number density field $\rho(\vec{r}')$, then Eq. (2) becomes

$$\vec{E}(\vec{r}) = r_e E_0 \int d\vec{r}' \rho(\vec{r}') [(\hat{n} \cdot \hat{\varepsilon}) \hat{n} - \hat{\varepsilon}] \frac{e^{i(k|\vec{r}-\vec{r}'| + \vec{k}_i \cdot \vec{r}')}}{|\vec{r} - \vec{r}'|}. \quad (4)$$

The domain of integration is the volume of intersection of the beam and the sample. (Here, and in what follows, we assume the origin of our coordinate system is at the center of the sample.) We now make several common simplifications to Eq. (4) in order to cast it into a more tractable form. Defining the lengths $r = |\vec{r}|$ and $r' = |\vec{r}'|$, the unit vectors $\hat{r} = \vec{r}/r$ and $\hat{r}' = \vec{r}'/r'$, and the parameter $\epsilon = r'/r$, the Taylor series of $1/|\vec{r} - \vec{r}'|$ and \hat{n} in powers of ϵ yield

$$\frac{1}{|\vec{r} - \vec{r}'|} = \frac{1}{r} [1 + \epsilon \hat{r} \cdot \hat{r}' + O(\epsilon^2)]$$

and

$$\hat{n} = \hat{r} + \epsilon [(\hat{r} \cdot \hat{r}') \hat{r} - \hat{r}'] + O(\epsilon^2),$$

respectively. If $\epsilon \ll 1$ then we may approximate these as $1/|\vec{r} - \vec{r}'| \approx 1/r$ and $\hat{n} \approx \hat{r}$, and Eq. (4) becomes

$$\vec{E}(\vec{r}) = E_0 \frac{r_e}{r} [(\hat{r} \cdot \hat{\varepsilon}) \hat{r} - \hat{\varepsilon}] \int d\vec{r}' \rho(\vec{r}') e^{i(k|\vec{r}-\vec{r}'| + \vec{k}_i \cdot \vec{r}')}. \quad (5)$$

Note that these approximations imply that $t/L \ll 1$ and $d/L \ll 1$.

The scattered intensity at \vec{r} is given by

$$\begin{aligned} I(\vec{r}) &= \frac{c}{8\pi} \langle |\vec{E}(\vec{r})|^2 \rangle \\ &= I_0 \left(\frac{r_e}{r} \right)^2 \langle |(\hat{r} \cdot \hat{\varepsilon}) \hat{r} - \hat{\varepsilon}|^2 \rangle |F(\vec{r})|^2, \end{aligned} \quad (6)$$

where we have used Eq. (5). Here $I_0 = cE_0^2/8\pi$ is the average intensity of the light source, the angle brackets $\langle \dots \rangle$ represent an average over the ensemble of possible polarization vectors \hat{e} , and the dimensionless, scalar field $F(\vec{r})$ is given by

$$F(\vec{r}) = \int d\vec{r}' \rho(\vec{r}') e^{i(k|\vec{r}-\vec{r}'| + \vec{k}_i \cdot \vec{r}')}. \quad (7)$$

For an unpolarized source, it can be shown that the polarization term becomes

$$\langle (\hat{r} \cdot \hat{e})\hat{r} - \hat{e} \rangle^2 = \frac{1}{2}(1 + (\hat{k}_i \cdot \hat{r})^2),$$

where $\hat{k}_i = \vec{k}_i/k$.

The integral in Eq. (7) cannot in general be solved analytically, and is not amenable to numerical fast Fourier transform (FFT) methods. The remainder of this section, and indeed much of the history of diffraction theory, consists of an exploration of various approximations to Eq. (7). Before we continue, it is worthwhile to note that in arriving at Eq. (7) we have neglected the possibility that the intensity may vary from point to point within the sample, due to the effects of both absorption and an imperfect radial beam profile. This is easily dealt with, however, by including a position-dependent intensity field $I(\vec{r})$:

$$F(\vec{r}) = \int d\vec{r}' \rho(\vec{r}') \sqrt{I(\vec{r}')/I_0} e^{i(k|\vec{r}-\vec{r}'| + \vec{k}_i \cdot \vec{r}')}.$$

However, the validity of the results in the remainder of this paper are unaffected by this term, and it will be omitted in what follows.

A. The classical far-field regime

The primary barrier to an analysis of the field in Eq. (7) is the presence of the nonlinear factor $k|\vec{r} - \vec{r}'|$ in the exponent. However, if we once again define the small parameter $\epsilon = r'/r$, and assume that L is much larger than the dimensions of the spot size d and sample thickness t , then we may perform a Taylor series of this factor as follows:

$$\begin{aligned} k|\vec{r} - \vec{r}'| &= k\sqrt{r^2 - 2\vec{r} \cdot \vec{r}' + r'^2} \\ &= kr\sqrt{1 - 2\epsilon\hat{r} \cdot \hat{r}' + \epsilon^2} \\ &= kr\left\{1 - \epsilon\hat{r} \cdot \hat{r}' + \epsilon^2\frac{1}{2}(1 - \hat{r} \cdot \hat{r}') + O(\epsilon^3)\right\} \\ &= kr - kr\underbrace{\frac{r'}{r}\hat{r} \cdot \hat{r}'}_{=k\hat{r} \cdot \hat{r}'} + kr\underbrace{\frac{r'^2}{r^2}\frac{1}{2}(1 - \hat{r} \cdot \hat{r}')}_{=\frac{kr'^2}{r}\frac{1}{2}(1 - \hat{r} \cdot \hat{r}')} + O(\epsilon^3). \end{aligned} \quad (8)$$

In order for the third term in Eq. (8) to be ignorable, it is insufficient that it merely be much smaller than all lower-order terms. Instead, it is necessary that this term contribute an ignorable phase (i.e., $\ll \pi$) to the complex exponential in Eq. (7). We first derive an upper bound on the size of this term:

$$\begin{aligned} \frac{kr'^2}{r}\frac{1}{2}(1 - \hat{r} \cdot \hat{r}') &\leqslant \frac{kr'^2}{r} \quad \text{because } 1 - \hat{r} \cdot \hat{r}' \leqslant 2 \\ &\leqslant \frac{kr'^2}{L} \quad \text{because } r \geqslant L \end{aligned}$$

$$\begin{aligned} &\leqslant \frac{1}{4} \frac{k(d^2 + t^2)}{L} \\ &\quad \text{because } r'^2 \leqslant \left(\frac{d}{2}\right)^2 + \left(\frac{t}{2}\right)^2 \\ &\leqslant \frac{1}{2} \frac{k \max(d, t)^2}{L} \\ &\quad \text{because } d^2 + t^2 \leqslant 2 \max(d, t)^2 \\ &\leqslant \frac{\pi}{\lambda L} \frac{\max(d, t)^2}{\lambda L} \quad \text{because } k = \frac{2\pi}{\lambda}. \end{aligned}$$

We assume at this point that $d \geqslant t$. Although this is not always the case, it simplifies subsequent expressions without significant loss of generality. The third term in Eq. (8) then contributes an ignorable phase if

$$\text{Fr} \equiv \frac{d^2}{\lambda L} \ll 1, \quad (9)$$

where Fr is the dimensionless *Fresnel number*. It can be shown that when $\text{Fr} \ll 1$, all higher order terms in Eq. (8) can likewise be ignored. In this limit, Eq. (7) becomes

$$F(\vec{r}) = F(\vec{q}) = e^{ikr} \int d\vec{r}' \rho(\vec{r}') e^{-i\vec{q} \cdot \vec{r}'}, \quad (10)$$

where the *scattering vector*

$$\vec{q} = \vec{q}(\vec{r}) \equiv \vec{k}_f - \vec{k}_i = k\hat{r} - \vec{k}_i \quad (11)$$

is the difference between the incoming (\vec{k}_i) and outgoing ($\vec{k}_f = k\hat{r}$) wave vectors of the scattered light.

Note that there is some variation in the literature with regard to which planes the Fresnel number is calculated with respect to. Whereas here we will always define the Fresnel number in terms of propagation from the sample plane to the detector plane, some authors (see, e.g., Quiney *et al.* [21] and Williams *et al.* [18]) calculate it with respect to propagation from the source plane to the sample plane. As such, these authors report relatively high Fresnel numbers—about 5 and about 28, respectively, for the two previous references—in their experiments (which take place very close to a small source). By a sample-to-detector Fresnel number calculation, however, their values of Fr are significantly lower, e.g., ~ 0.01 to 0.30 for Williams *et al.* (wherein it is made clear that the detector is indeed in the far field of the sample).

Together, Eqs. (9) and (10) define the classical *far-field*, or Fraunhofer, regime of diffraction. In this regime, the field $F(\vec{q})$ is simply a Fourier transform of the electron number density field $\rho(\vec{r})$ in the sample. This makes diffraction in the far field highly amenable to both theoretical and numerical analysis. In particular, the fact that FFT techniques can be applied to the evaluation of Eq. (10) is especially fortuitous for imaging applications and the simulation of x-ray diffraction experiments (see Sec. III). The Fresnel number itself is a ratio of two other ratios: d/L and λ/d . It is useful to think of the double-slit interference problem, in which the slit size is generally greater than the wavelength.

B. The Fresnel regime

At the high photon energies E_γ (and hence small wavelengths λ) and large spot sizes d required for the imaging of higher- Z materials, achieving a Fresnel number $\text{Fr} \ll 1$ is impossible without requiring prohibitively large sample-detector distances L (i.e., kilometers). When $\text{Fr} \ll 1$, we are said to be in the *Fresnel regime* of diffraction. It is often thought that one *must* be in the far-field regime to generate meaningful diffraction patterns. In fact, this is not true, and it can be shown that a useful approximation of Eq. (7) valid in the Fresnel regime follows from Huygens' principle [19,22], and a diffractive imaging method based on this approximation has been proposed [23]. In this section, we describe the relevant theory.

A different approximation can be applied to the quantity $k|\vec{r} - \vec{r}'|$ which is known as the *small-angle approximation* in the optics literature. The vector \vec{r} extends from the origin at the center of the sample to a point on the detector. Assuming, as before, that the detector is centered on the positive z axis, we can decompose \vec{r} as $\vec{r} = L\hat{e}_z + \vec{r}_\perp$, where $L\hat{e}_z$ is the component of \vec{r} parallel to the beam direction, and \vec{r}_\perp is the component parallel to the detector's surface. (Note that, Fig. 1 notwithstanding, the detector's surface need not in general be entirely perpendicular to the z axis; i.e., it may be tilted or curved, so that $\hat{e}_z \cdot \vec{r}_\perp \neq 0$.) With this definition, we have

$$\begin{aligned} k|\vec{r} - \vec{r}'| &= k|L\hat{e}_z + \vec{r}_\perp - \vec{r}'| \\ &= kL\left|\hat{e}_z + \frac{\vec{r}_\perp - \vec{r}'}{L}\right| \\ &= kL\sqrt{1 + 2\hat{e}_z \cdot \left(\frac{\vec{r}_\perp - \vec{r}'}{L}\right) + \left|\frac{\vec{r}_\perp - \vec{r}'}{L}\right|^2}. \end{aligned} \quad (12)$$

The small-angle approximation is realized when the length of the dimensionless vector $(\vec{r}_\perp - \vec{r}')/L$ is small. We consider two different cases.

I. Two-dimensional samples

The mathematical analysis of diffraction in the Fresnel regime has historically focused exclusively on the consideration of two-dimensional samples, i.e., very thin samples or apertures in an otherwise opaque barrier (e.g., the aforementioned double-slit experiment). In such problems, the electron number density field $\rho(\vec{r}')$ appearing in expressions such as Eq. (7) has units of 1/area rather than the usual 1/volume. We assume in this case that the sample lies entirely in the xy plane, so that the source point integration variable \vec{r}' satisfies $\hat{e}_z \cdot \vec{r}' = 0$. Furthermore, we assume that the detector's surface is entirely perpendicular to the z axis, so that $\hat{e}_z \cdot \vec{r}_\perp = 0$. In this case, Eq. (12) becomes

$$\begin{aligned} k|\vec{r} - \vec{r}'| &= kL\sqrt{1 + \left|\frac{\vec{r}_\perp - \vec{r}'}{L}\right|^2} \\ &= kL\left\{1 + \frac{1}{2}\left|\frac{\vec{r}_\perp - \vec{r}'}{L}\right|^2 - \frac{1}{8}\left|\frac{\vec{r}_\perp - \vec{r}'}{L}\right|^4\right. \\ &\quad \left.+ O\left(\left|\frac{\vec{r}_\perp - \vec{r}'}{L}\right|^6\right)\right\}. \end{aligned} \quad (13)$$

We wish to derive the conditions under which the third term in Eq. (13) can safely be ignored. An upper bound on its magnitude may be derived as follows:

$$\begin{aligned} kL \frac{1}{8}\left|\frac{\vec{r}_\perp - \vec{r}'}{L}\right|^4 &= \frac{\pi}{4} \frac{1}{\lambda L^3} |\vec{r}_\perp - \vec{r}'|^4 \quad \text{because } k = \frac{2\pi}{\lambda} \\ &\leq \frac{\pi}{4} \frac{1}{\lambda L^3} (|\vec{r}_\perp| + |\vec{r}'|)^4 \\ &\quad \text{by the triangle inequality} \\ &\leq \frac{\pi}{4} \frac{1}{\lambda L^3} \left(\frac{D}{\sqrt{2}} + \frac{d}{2}\right)^4 \\ &\quad \text{because } |\vec{r}_\perp| \leq \frac{D}{\sqrt{2}} \quad \text{and } |\vec{r}'| \leq \frac{d}{2} \\ &\leq \frac{\pi}{4} \left(\frac{1}{\sqrt{2}} + \frac{1}{2}\right)^4 \frac{D^4}{\lambda L^3} \quad \text{assume } d \leq D. \end{aligned}$$

As in Sec. II A, this term contributes an ignorable phase to the complex exponential in Eq. (7) if its magnitude is $\ll \pi$, a condition which obtains when

$$\text{An} \equiv \frac{D^4}{\lambda L^3} \ll 1, \quad (14)$$

where we have ignored the order-unity factor $(1/2 + 1/\sqrt{2})^4/4 \approx 0.53$. This defines the *small-angle number* An , the value of which determines whether the neglect of the third term—and all higher terms—in Eq. (13) is a valid approximation. This quantity has previously been alluded to (although not by name) in Römer [24]. Note that whether a given experiment satisfies Eq. (14) is typically independent of whether the Fresnel number is small. Furthermore, the small-angle number An can be large even when the relevant angle is small; thus $\text{An} \ll 1$ is a more stringent requirement than the small-angle condition that $D/L \ll 1$.

Noting that the second term in brackets in Eq. (13) yields

$$\begin{aligned} kL \frac{1}{2}\left|\frac{\vec{r}_\perp - \vec{r}'}{L}\right|^2 &= \frac{k}{2L} (|\vec{r}_\perp|^2 + |\vec{r}'|^2 - 2\vec{r}_\perp \cdot \vec{r}') \\ &= \frac{k}{2L} (|\vec{r}_\perp|^2 + |\vec{r}'|^2 - 2(L\hat{e}_z + \vec{r}_\perp) \cdot \vec{r}') \\ &\quad \text{because } \hat{e}_z \cdot \vec{r}' = 0 \\ &= \frac{k}{2L} (|\vec{r}_\perp|^2 + |\vec{r}'|^2 - 2\vec{r} \cdot \vec{r}') \\ &\quad \text{because } \vec{r} = L\hat{e}_z + \vec{r}_\perp \end{aligned}$$

in the $\text{An} \ll 1$ limit, Eq. (7) becomes

$$F(\vec{r}) = F(\vec{K}) = e^{i(kL + \frac{k|\vec{r}_\perp|^2}{2L})} \int d\vec{r}' \bar{\rho}(\vec{r}') e^{-i\vec{K} \cdot \vec{r}'}, \quad (15)$$

where the Fresnel regime scattering vector is

$$\vec{K} = \vec{K}(\vec{r}) \equiv k \frac{\vec{r}}{L} - \vec{k}_i, \quad (16)$$

and

$$\bar{\rho}(\vec{r}') \equiv \rho(\vec{r}') e^{i\frac{k|\vec{r}'|^2}{2L}} \quad (17)$$

is the “distorted object” density field proposed in Xiao and Shen [23]. Note that the complex exponential factor that multiplies the electron density field in Eq. (17) has a phase of order the Fresnel number. In the classical far-field limit of small Fr this exponential phase factor thus approaches unity and the necessity of considering a “distorted object” is removed.

2. Three-dimensional samples

The results of the previous section apply only to two-dimensional samples with diffraction patterns projected onto flat detectors perpendicular to the z axis. For three-dimensional samples, these results are not valid for imaging applications since the scattering vector \vec{K} has no components in the z direction:

$$\begin{aligned}\hat{e}_z \cdot \vec{K} &= \frac{k}{L} \hat{e}_z \cdot \vec{r} - \hat{e}_z \cdot \vec{k}_i \\ &= \frac{k}{L} \hat{e}_z \cdot (L \hat{e}_z + \vec{r}_\perp) - k \\ &= \frac{k}{L} \hat{e}_z \cdot \vec{r}_\perp = 0.\end{aligned}$$

Thus no Fourier information about variation of the sample in the z direction is preserved in the diffraction pattern, and imaging of three-dimensional samples in this regime is reduced to the imaging of a projection of the sample onto a two-dimensional plane perpendicular to z . Nevertheless, the final equality above raises a question: Can we change the geometry of the experiment by tilting or curving the detector, so that $\hat{e}_z \cdot \vec{r}_\perp \neq 0$, which would in turn allow the scattering vector to take on nonzero z components? In fact, this is *not* possible, as we demonstrate below.

In three-dimensional samples, for a general source point \vec{r}' within the sample, $\hat{e}_z \cdot \vec{r}' \neq 0$. Assuming in addition that for a general value of \vec{r}_\perp on the detector, $\hat{e}_z \cdot \vec{r}_\perp \neq 0$, we return to Eq. (12) and perform a Taylor series of $k|\vec{r} - \vec{r}'|$ in powers of $|(\vec{r}_\perp - \vec{r}')/L|$:

$$\begin{aligned}k|\vec{r} - \vec{r}'| &= kL \left\{ 1 + \hat{e}_z \cdot \left(\frac{\vec{r}_\perp - \vec{r}'}{L} \right) \right. \\ &\quad + \frac{1}{2} \left(\left| \frac{\vec{r}_\perp - \vec{r}'}{L} \right|^2 - \left[\hat{e}_z \cdot \left(\frac{\vec{r}_\perp - \vec{r}'}{L} \right) \right]^2 \right) \\ &\quad + \frac{1}{2} \left(\left[\hat{e}_z \cdot \left(\frac{\vec{r}_\perp - \vec{r}'}{L} \right) \right]^3 \right. \\ &\quad \left. - \hat{e}_z \cdot \left(\frac{\vec{r}_\perp - \vec{r}'}{L} \right) \left| \frac{\vec{r}_\perp - \vec{r}'}{L} \right|^2 \right) \\ &\quad \left. + O\left(\left| \frac{\vec{r}_\perp - \vec{r}'}{L} \right|^4\right) \right\}. \quad (18)\end{aligned}$$

It can be shown that the fourth term in curly brackets above (the third-order term) contributes an ignorable phase to the complex exponential in Eq. (7), and may be ignored along with all higher-order terms, if

$$\frac{D^2}{\lambda L^2} \max(t, D \sin \chi) \ll 1,$$

where χ is the largest angular deviation that \vec{r}_\perp achieves as a result of the tilt or curvature of the detector’s surface.

Collecting the remaining terms, we are left with

$$\begin{aligned}k|\vec{r} - \vec{r}'| &= k \left[L + \hat{e}_z \cdot \vec{r}_\perp + \frac{1}{2L} (|\vec{r}_\perp|^2 - (\hat{e}_z \cdot \vec{r}_\perp)^2) \right] \\ &\quad + \frac{k}{2L} (|\vec{r}'|^2 - z') - k \left(\hat{e}_z + \frac{\vec{r}_\perp}{L} - \frac{\hat{e}_z \cdot \vec{r}_\perp}{L} \hat{e}_z \right) \cdot \vec{r}',\end{aligned}$$

and Eq. (7) becomes

$$F(\vec{r}) = e^{i[k(L + \hat{e}_z \cdot \vec{r}_\perp + \frac{1}{2L}(|\vec{r}_\perp|^2 - (\hat{e}_z \cdot \vec{r}_\perp)^2))]} \int d\vec{r}' \bar{\rho}(\vec{r}') e^{-i\vec{K} \cdot \vec{r}'},$$

where the new scattering vector is

$$\vec{K} \equiv k \left(\hat{e}_z + \frac{\vec{r}_\perp}{L} - \frac{\hat{e}_z \cdot \vec{r}_\perp}{L} \hat{e}_z \right) - \vec{k}_i,$$

and

$$\bar{\rho}(\vec{r}') \equiv \rho(\vec{r}') e^{i \frac{k}{2L} (|\vec{r}'|^2 - z'^2)}.$$

It is straightforward to show that despite the improved generality of the above approach, it is still the case that $\hat{e}_z \cdot \vec{K} = 0$, and therefore no imaging z resolution is captured by a diffraction pattern governed by such an approximation. This can be explained geometrically by noting that limitation to a small scattering angle implies that in Fresnel regime imaging the curvature of the Ewald sphere has been neglected, along with the sample depth information it encodes [25].

It should be emphasized that expressions such as Eq. (15) or Eq. (10) are merely approximations to the process of diffraction pattern formation, formulated for easier analysis. In reality, diffraction patterns form according to the more exact expression (7) [or, even better, (4)]. In contrast to Eq. (15), these expressions do contain z information, whatever regime one is in. This fact has been demonstrated in the so-called “ankylography” technique, which relies upon the curvature of the Ewald sphere in the far field to obtain three-dimensional imaging from a single exposure angle [25–27]. If iterative phase retrieval using Eqs. (7) or Eqs. (4) were possible, then three-dimensional information might be extracted even in the more stringent geometries described in this work.

III. COHERENT X-RAY DIFFRACTION IMAGING

Equations (10) and (15) both stem from approximations that allow the diffraction pattern to be represented in terms of a Fourier transform of the original object, possibly modified by a complex form factor. Coherent x-ray diffraction imaging (CXDI) is a lensless imaging technique which exploits this simple Fourier relationship to reconstruct a two- or three-dimensional image of the sample from its coherent diffraction pattern. However, the detector preserves only the amplitude, and not the phase, of the scattered field, a difficulty referred to as the “missing phase problem” [7]. A numerical process known as iterative phase retrieval (IPR) must therefore be used to recover this missing phase information [4,28]. IPR requires that the diffraction pattern be *oversampled* [29] at a greater resolution than is nominally sufficient according to Nyquist theory. In this section we provide an overview of the details of CXDI and then apply that to understanding geometry and detector limitations that occur in mesoscale imaging.

A. Imaging resolution

The set of scattering vectors \vec{q} subtended by the detector's surface characterizes the imaging resolution of CXDI. At every point on the detector, we can divide \vec{q} into components parallel and perpendicular to the original beam direction. We define q_{\perp}^{\max} and q_{\parallel}^{\max} as the maximum magnitude these perpendicular and parallel components achieve, respectively, for a given experimental geometry. From Fig. 1 and the definition of \vec{q} in Eq. (11), it is straightforward to show that

$$q_{\perp}^{\max} = \frac{2\pi}{\lambda} \sin \phi = \frac{2\pi}{\lambda} \frac{D/2}{\sqrt{(\frac{D}{2})^2 + L^2}} \approx \frac{\pi D}{\lambda L} \quad (19)$$

and

$$\begin{aligned} q_{\parallel}^{\max} &= \frac{2\pi}{\lambda} (1 - \cos \phi) = \frac{2\pi}{\lambda} \left(1 - \frac{L}{\sqrt{(\frac{D}{2})^2 + L^2}} \right) \\ &\approx \frac{\pi}{4} \frac{D^2}{\lambda L^2}, \end{aligned} \quad (20)$$

where the latter approximations assume that $D \ll L$. (It should be noted that in the two-dimensional Fresnel regime, we can similarly define K_{\perp}^{\max} , which takes the value $\pi D/\lambda L$ exactly.) When performing CXDI in three dimensions, one has two different resolutions in the reconstructed image of the sample: a transverse resolution Δx perpendicular to the beam direction, and a longitudinal resolution Δz parallel to the beam direction. These are related to q_{\perp}^{\max} and q_{\parallel}^{\max} by

$$q_{\perp}^{\max} = \frac{2\pi}{2\Delta x} = \frac{\pi}{\Delta x} \quad (21)$$

and

$$q_{\parallel}^{\max} = \frac{2\pi}{2\Delta z} = \frac{\pi}{\Delta z}. \quad (22)$$

Note in particular the additional factor of 2 in the denominators of the middle expressions in Eqs. (21) and (22). This is the often-overlooked Nyquist factor, which stems from the fact that the smallest wavelength represented by a grid-sampled function is *twice* the grid size. Combining Eqs. (19)–(22) yields expressions for the resolutions Δx and Δz in terms of the experimental geometry:

$$\frac{\Delta x}{\lambda} = \frac{1}{D} \sqrt{\left(\frac{D}{2}\right)^2 + L^2} \approx \frac{L}{D}, \quad (23)$$

$$\frac{\Delta z}{\lambda} = \frac{1}{2} \left(1 - \frac{L}{\sqrt{(\frac{D}{2})^2 + L^2}} \right)^{-1} \approx \frac{4L^2}{D^2}, \quad (24)$$

where the latter approximations once again assume that $D \ll L$. The above expressions imply that the transverse and longitudinal resolutions Δx and Δz are not independent. Combining Eqs. (23) and (24) yields

$$\frac{\Delta z}{\lambda} = \frac{1}{2} \left(1 - \frac{\sqrt{(2\Delta x/\lambda)^2 - 1}}{2\Delta x/\lambda} \right)^{-1} \approx 4 \left(\frac{\Delta x}{\lambda} \right)^2. \quad (25)$$

For reasons related to the Nyquist explanation above, Δx is always greater than $\lambda/2$. Equation (25) therefore implies that

the longitudinal resolution is always worse (i.e., larger) than the transverse resolution.

B. Imaging geometry

We have demonstrated how the experimental parameters determine the imaging *resolution*. In fact, they also determine the imaging *geometry*, i.e., the size and shape of the region nominally described by the diffraction pattern. In order for the integral in Eq. (7) to be representable as a Fourier transform, upon which iterative phase retrieval can then be performed, either $\text{Fr} \ll 1$ [Eq. (9)] or $\text{An} \ll 1$ [Eq. (14)]. For mesoscale imaging, the illuminated spot size d is large and, as we will show later, the photon energy required to penetrate thick samples makes the photon wavelength λ small. Hence, unless extremely long detector beam lines L are built, $\text{Fr} > 1$. The primary constraint on mesoscale imaging then comes from the requirement that the small-angle approximation remain valid. Again, for not unreasonable detector beam lines L and very short wavelengths λ , this limits the full detector extent D or equivalently the maximum scattering angle and hence the minimum spatial resolution [Eq. (23)] that can be measured by diffractive imaging.

The height/width and thickness of the *computational domain* for iterative phase retrieval are given by $O_{\perp}d$ and $O_{\parallel}t$, respectively, where O_{\perp} is the *transverse oversampling factor* and O_{\parallel} is the *longitudinal oversampling factor*. In general, O_{\perp} and O_{\parallel} cannot be specified independently. The set of scattering vectors \vec{q} captured by the detector is not a continuum, but rather a discrete set, with the (generally nonuniform) increments of \vec{q} determined by the detector position and pixel size. The maximum size of these increments in the transverse and longitudinal directions determine O_{\perp} and O_{\parallel} , respectively. For the simple geometry shown in Fig. 1, and assuming $D \ll L$, it can be shown that

$$O_{\perp}d \approx \frac{\lambda L}{p} \quad (26)$$

and

$$O_{\parallel}t \approx \frac{2\lambda L^2}{pD} = \frac{2L}{D} O_{\perp}d. \quad (27)$$

There is a subtlety here. In real applications, one takes the nonuniform scattering vector samples measured by the detector and embeds them into a two- or three-dimensional rectangular grid. There is considerable freedom in choosing the spacings of this grid, so long as its Fourier-space resolution is not better than that of the original diffraction pattern. For example, in Raines *et al.* [25], 3×3 groupings of pixels were averaged to reduce noise, resulting in an effective pixel size $p_{\text{eff}} = 3p$. In practice, therefore, Eqs. (26) and (27) represent upper bounds on the oversampling factors and computational domain sizes accessible to the experiment.

C. Detector limitations on the field of view

From Eq. (26), the choice of the spot size d is a trade-off between the maximum feasible sample-detector distance L and the minimum available pixel size p for a given wavelength λ . Increasing the spot size reduces the scattering angle corresponding to the scale of d , and for a given pixel size the

detector must therefore be moved further back to oversample at that scale. Advances in small pixel technology can therefore save money on conventional facilities by reducing the required value of L . Conversely, conservative decisions on detector technology (i.e., assuming large pixels) will limit the field of view (the sample illumination spot size) given limitations on the detector hall. One might use an optic on the scattered light side of the sample made of a simple hemisphere of any low-absorbing material, such as Be. This would expand the divergence angle of the scattered light, effectively optically increasing L . Since the interference pattern is “formed” in the sample, any optic that follows is only redirecting rays. This sets an optic requirement of limiting the optic imperfections so that a perceptible overlap of adjacent rays does not occur at the detector. This is much less stringent than maintaining the transverse coherence before the sample, implies that surface imperfections will not matter, and should be easily fabricated.

By having a pixel size $p = \lambda L / O_{\perp} d$ one is effectively making measurements at a larger spot size than was actually illuminated. The result is that the region to be imaged, the spot size d , corresponds to a region in the Fourier plane (i.e., the detector) O_{\perp} pixels across, while the minimum size to be resolved, the transverse spatial resolution Δx , is determined for fixed L by the detector size D . The “imaging figure-of-merit” iFOM is defined as the transverse field of view (or spot size) divided by the transverse spatial resolution,

$$\text{iFOM} = \frac{d}{\Delta x} \approx \frac{D}{O_{\perp} p}, \quad (28)$$

where in arriving at the last approximate equality, we have made use of Eqs. (23) and (26).

There is a further requirement on the relative bandwidth, $\Delta\lambda/\lambda$, of the “monochromatic” source. Each feature in a diffraction pattern will have a certain spread in size on the detector because of the bandwidth or energy variation of the source. The largest spread (which occurs near the edge of the detector measuring the smallest scales) needs to be smaller than a pixel size, leading to a requirement [30] of

$$\frac{\Delta\lambda}{\lambda} < \frac{\Delta x}{O_{\perp} d} = \frac{1}{O_{\perp} \text{iFOM}}. \quad (29)$$

For example, with a 100 micron diameter spot size and desired imaging resolution of 100 nanometers (an iFOM = 1000) and an oversampling $O_{\perp} = 2$ the bandwidth must be better than $\Delta\lambda/\lambda < 5 \times 10^{-4}$.

D. Iterative phase retrieval

As mentioned in the introduction of this section, only the scattered amplitudes—but not the phases—are measured by a detector. Provided that $O_{\perp}^2 > 2$ in two dimensions or $O_{\perp}^2 O_{\parallel} > 2$ in three dimensions, this missing information can in principle be retrieved by IPR. Here we provide an outline of IPR algorithms for two-dimensional imaging applications, as can be found in reviews such as those of Chapman and Nugent [4], Abbey [5], or Marchesini [31].

One starts with the intensities measured by the $N_p \times N_p$ pixels on the detector, which correspond to amplitudes of the Fourier transform of the density field in the $O_{\perp} d \times O_{\perp} d$ computational domain. If necessary, this set of amplitudes is

interpolated onto a regular $N_p \times N_p$ complex grid. Random phases are assigned to each point, and an inverse FFT is performed which transforms the data to the spatial, or image, plane. Since $O_{\perp} d > d$, any electron number density in the reconstructed image which is outside the actual $\sim d \times d$ area of the spot will be set to zero. Densities within the spot are left unaffected. (This step is termed “applying the support,” and could also involve the enforcement of other known constraints on the predicted density field, such as radiography data.) Now a FFT is performed which returns us to the Fourier, or detector, plane. All amplitudes are set back to those implied by the observed diffraction pattern, but the new predicted phases are retained. This process is iterated until convergence is achieved and a reconstructed sample image is obtained, which may take anywhere from tens to tens of thousands of iterations, depending on the algorithmic variant employed, the noise level, and the details of the sample. It can be shown that convergence is guaranteed for all but a pathological set of possible samples [32]. See Fig. 3 for examples of this process performed at several Fresnel numbers using a simulated sample and diffraction patterns. (Note that it is a general empirical observation in calculations of this type—see also Xiao and Shen [23]—that IPR tends to converge more rapidly at higher Fresnel number.)

IV. CHOICE OF PHOTON ENERGY

At the mesoscale “the extremes of heterogeneity in a material dominate performance at the expense of the homogeneous bulk” [2], and it is necessary to allow multiple measurements on single samples each of which has different rare events and fluctuations in defects. Especially in dynamic extremes, the choice of the light source photon energy is a delicate trade-off between maximization of the coherently scattered signal, and minimizing the heating of the illuminated spot to make multiple measurements. In this section, we explore both of these issues.

A. Optimizing the coherently scattered signal

Consider a coherent photon bunch consisting of N_0 photons traveling in the z direction and impinging upon a sample. A given photon in the bunch has a number of possible fates: It may pass through the sample unaffected, it may be absorbed (photoelectric absorption, in which the photon’s entire energy E_{γ} is transferred to the sample), it may be scattered incoherently (inelastic, or Compton, scattering, in which a fraction of the photon’s energy is transferred to the sample, depending on the scattering angle), it may be scattered coherently (elastic, or Thomson, scattering, in which none of the photon’s energy is transferred to the sample), etc. It may also be subject to some combination of these events: It may be scattered and then absorbed, it may be scattered coherently twice, etc. In general, the history of a given photon can be treated as a continuous Markov process, with Poisson-distributed transition times mediated by the relevant cross sections of the material at the given photon energy. The relevant cross sections include those for photoelectric absorption, coherent scattering, incoherent scattering, as well

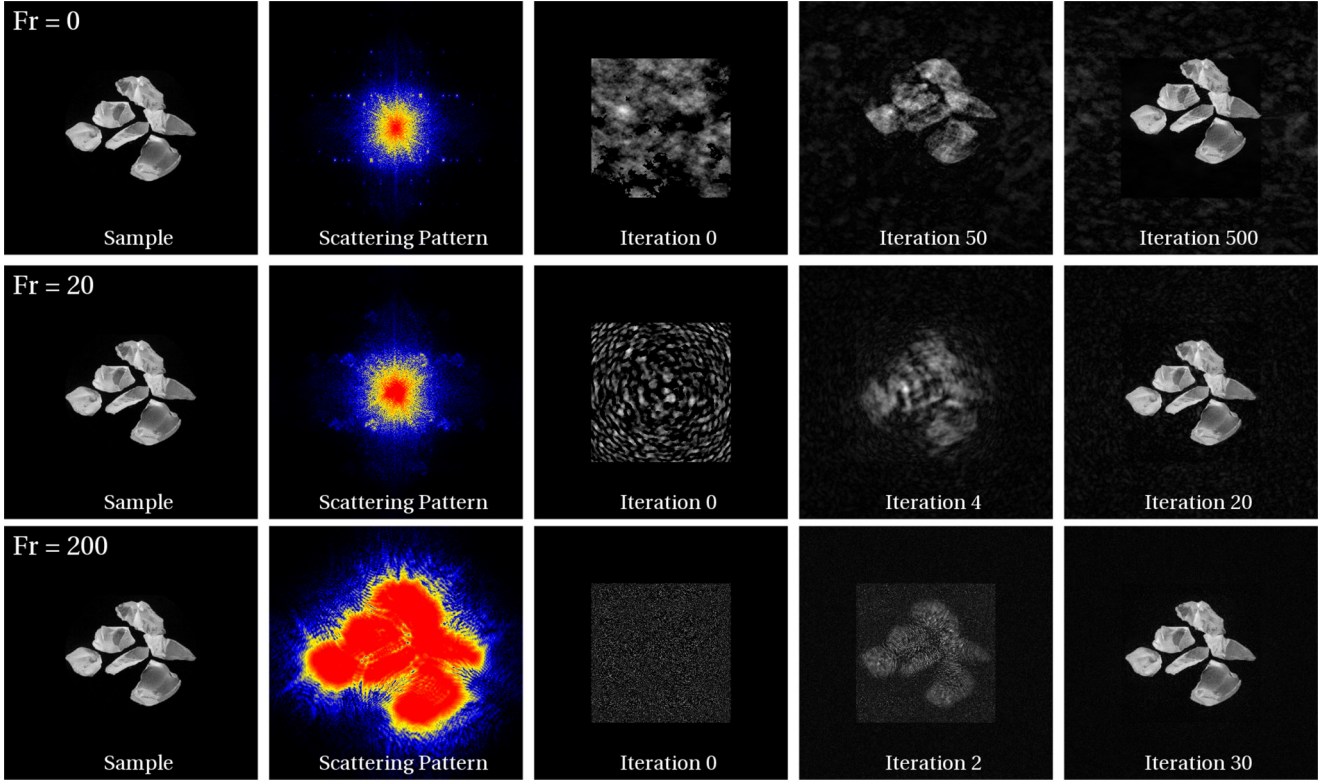


FIG. 3. (Color online) Examples of simulated x-ray scattering and iterative phase retrieval using a model 2D sample at different Fresnel numbers ($Fr = 0, 20$, and 200 from top to bottom).

as that for total attenuation, which is the sum of the preceding three. In CXDI, we wish to maximize the signal resulting from those photons which, from their original unscattered and unabsorbed state, have coherently scattered once and only once. How many of these particular photons are present in the beam at a given penetration depth z into the sample? Equivalently, how many such photons will emerge from a sample with a total thickness t ?

The various relevant cross sections are usually tabulated in units of area per unit mass. Let σ_T and σ_C be the cross sections per unit mass for total attenuation and coherent scattering, respectively. Examples of σ_T and σ_C taken from the online NIST XCOM photon cross sections database [33] are shown in Fig. 4. If ρ_m is the average mass density of the sample, then the exponential *attenuation coefficients* for total attenuation and coherent scattering are defined as $\mu_T = \sigma_T \rho_m$ and $\mu_C = \sigma_C \rho_m$, respectively. Note that these quantities have units of inverse length. We define $N_U(z)$ as the number of unscattered and unabsorbed photons in the beam at penetration depth z . We further define $N_{1C}(z)$ as the number of photons in the beam at depth z whose only transition has been to coherently scatter once and only once. Clearly, $N_U(0) = N_0$ and $N_{1C}(0) = 0$. What are the rates at which $N_U(z)$ and $N_{1C}(z)$ change with z ? Any interaction whatsoever, be it scattering or absorption, will decrease $N_U(z)$. By definition the rate at which this occurs is $-\mu_T N_U(z)$. The situation for $N_{1C}(z)$ is slightly more complicated, as there are two ways in which $N_{1C}(z)$ may change. It can increase via the coherent scattering of previously unscattered and unabsorbed photons. This occurs at a rate of $+\mu_C N_U(z)$. It can also decrease via any interaction whatsoever

on the part of single-coherently-scattered photons. This occurs at a rate $-\mu_T N_{1C}(z)$.

Combining all of these expressions yields a pair of partially coupled differential equations for $N_U(z)$ and $N_{1C}(z)$:

$$\begin{aligned} \frac{d}{dz} N_U(z) &= -\mu_T N_U(z), \quad N_U(0) = N_0, \\ \frac{d}{dz} N_{1C}(z) &= -\mu_T N_{1C}(z) + \mu_C N_U(z), \quad N_{1C}(0) = 0. \end{aligned} \quad (30)$$

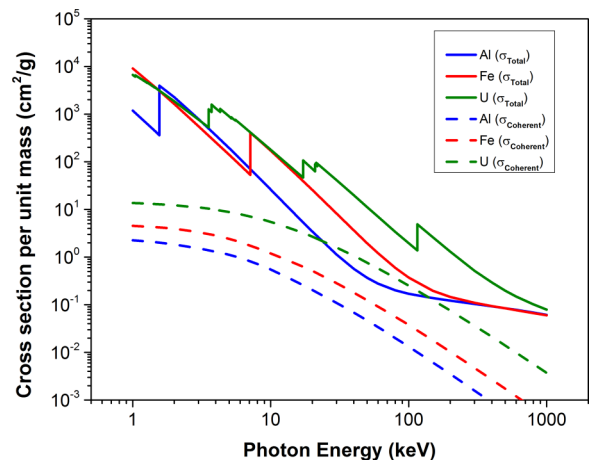


FIG. 4. (Color online) The total (solid) and elastic or coherent (dashed) cross sections per unit mass for uranium (green), iron (red), and aluminum (blue).

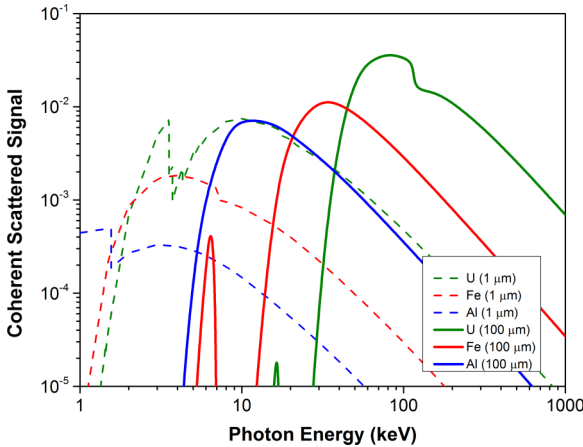


FIG. 5. (Color online) The fraction of incident photons coherently scattered just once, the coherent scattering signal N_{1C}/N_0 , as a function of incident photon energy for various materials at thicknesses of $1 \mu\text{m}$ (dashed lines) and $100 \mu\text{m}$ (solid lines), from Eq. (31).

Solving this set of equations and letting $z = t$, the thickness of the sample, yields the following expression for $N_{1C}(t)$:

$$N_{1C}(t) = N_0 \mu_C t e^{-\mu_T t}. \quad (31)$$

Note that when the sample thickness t tends to zero, although the transmission of the photons becomes unity, the number of photons that have coherently scattered goes proportionately to zero. $N_{1C}(t)$ has a maximum at $t_{\max} = 1/\mu_T$ of

$$N_{1C}(t_{\max}) = \frac{\mu_C}{\mu_T} \frac{N_0}{e}.$$

However, this optimal thickness is generally too thin to be practical for the materials and energies needed for mesoscale imaging. Instead, we must specify an experimentally feasible sample thickness t , and vary the photon energy E_γ (upon which μ_T and μ_C depend) to find the optimum value that maximizes the expression in Eq. (31) for the coherent signal. The results of such an analysis for various materials are shown in Fig. 5.

B. Expected heating of the spot

1. Temperature rise in samples

The energy absorbed in a sample E_{abs} depends on the total number of incident photons N_0 of photon energy E_γ and the total energy absorption coefficient μ_E that takes into explicit account (a) the emission of bremsstrahlung, (b) positron annihilation in flight, (c) fluorescence emission as a result of electron- and positron-impact ionization, and (d) the effects on these processes of energy-loss straggling and knock-on electron production as the secondary particles slow down. The energy absorption coefficient is smaller by about 80% than the total attenuation coefficient μ_T because some inelastic processes do not deposit the full photon energy in the sample. Then the absorbed energy is

$$E_{\text{abs}} = N_0 E_\gamma (1 - e^{-\mu_E t}), \quad (32)$$

where t is the sample thickness. Hence for thick samples, all the photons are absorbed.

TABLE I. Properties of some selected materials. Source: Ref. [34].

Material	Melting Temperature T_{melt} (K)	Mass Density ρ_m ($\frac{\text{g}}{\text{cm}^3}$)	Thermal Diffusivity α ($10^{-5} \frac{\text{m}^2}{\text{s}}$)	Volumetric Heat Capacity C_V ($10^6 \frac{\text{J}}{\text{m}^3 \text{K}}$)
Al	933.4	2.699	8.4	2.42
Fe	1811	7.87	2.3	3.53
Ti	1941	4.50	0.931	2.35
Cu	1358	8.96	11.2	3.45
U	1408	18.95	1.25	2.22

The number of singly scattered coherent photons required to be detected, which we denote by N_{req} , depends on the desired average number P of detected photons per pixel, the total number of pixels [$= (O_\perp \text{iFOM})^2$ from Eq. (28)], and the detector quantum efficiency η_{QE} . Combining these quantities yields $N_{\text{req}} = P (O_\perp \text{iFOM})^2 / \eta_{QE}$. Setting this detection requirement equal to the number of coherently scattered photons from the entire sample [Eq. (31)] determines the total number of incident photons required to make the measurement,

$$N_0 = \frac{P (O_\perp \text{iFOM})^2}{\eta_{QE} \mu_C t e^{-\mu_T t}}. \quad (33)$$

Combining Eqs. (32) and (33) yields the total energy going into heating:

$$E_{\text{abs}} = \frac{P (O_\perp \text{iFOM})^2 E_\gamma}{\eta_{QE}} \frac{1 - e^{-\mu_E t}}{\mu_C t e^{-\mu_T t}}. \quad (34)$$

We assume a sample of illuminated volume $V \approx \pi(d/2)^2 t$, atomic weight A , mass density ρ_m , and a volumetric heat capacity C_V . For cold crystalline materials, C_V is well-approximated for scaling purposes as three times the Boltzman constant k_B times the number of atoms per unit volume in the sample, i.e., $C_V \approx 3N_A \rho_m k_B / A$, where N_A is Avogadro's number. (One can use measured C_V values, which take into account how many degrees of freedom the temperature has compared to the photon energy, for better estimates. See, e.g., Table I.) Combining this with Eq. (34), we find that the average temperature rise in the sample is

$$\Delta T = \frac{E_{\text{abs}}}{\pi(d/2)^2 t C_V} = \frac{P (O_\perp \text{iFOM})^2 A}{3\pi(d/2)^2 N_A \rho_m k_B \eta_{QE}} \frac{E_\gamma (1 - e^{-\mu_E t})}{\mu_C t^2 e^{-\mu_T t}}. \quad (35)$$

The extra power of thickness in the denominator comes from the volume of atoms in the sample size over which the heating can be averaged. For samples thin compared to the shortest radiation length [the inverse of the largest attenuation coefficient in Eq. (35), generally $1/\mu_T$], the temperature rise is proportional to the imaging terms [$P (O_\perp \text{iFOM})^2 / \eta_{QE}$] times terms dependent on the photon energy and the element [$E_\gamma A \mu_E / (\rho_m \mu_C)$] times $1/t$. This divergence with decreasing t stems from Eq. (31): As the sample thickness decreases, more and more incident photons (and hence more heating) are required in order to produce the required number of photons to make the desired imaging measurement.

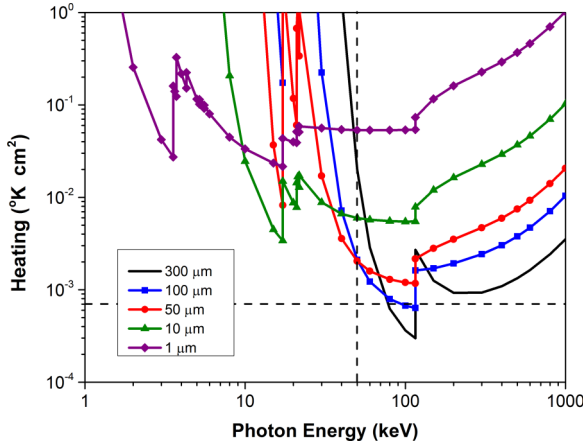


FIG. 6. (Color online) Average sample heating ΔT times the area of the illuminated spot $\pi(d/2)^2$ vs photon energy E_γ for uranium samples of various thicknesses. For reference, a photon energy of 50 keV is marked as a vertical dashed line, which crosses the 10, 50, and 100 μm curves at 6.0×10^{-3} , 2.0×10^{-3} , and $2.1 \times 10^{-3} \text{ K cm}^2$, respectively. The horizontal dashed line represents a 10 K temperature rise for a 100 μm diameter spot.

As an example, we present numbers for uranium ($A = 238.02891$, $\rho_m = 18.95 \text{ g/cm}^3$), which at $E_\gamma = 50 \text{ keV}$ has $\sigma_T = 11.21 \text{ cm}^2/\text{g}$, $\sigma_C = 0.7681 \text{ cm}^2/\text{g}$, and $\sigma_E = 9.034 \text{ cm}^2/\text{g}$. We assume a spot diameter $d = 100 \mu\text{m}$, a sample thickness $t = 100 \mu\text{m}$, $O_\perp = 2$, iFOM = 500, $P = 100$ detected photons per pixel, and $\eta_{QE} = 90\%$. Under these assumptions, Eq. (35) yields $\Delta T = 27 \text{ K}$. Note that this is the *average* temperature rise throughout the volume of a sample of thickness t . The *maximum* temperature rise will be on the front surface and higher by a factor of $\mu_E t / (1 - e^{-\mu_E t})$, which is approximately 2.1 for this thickness and material. Figure 6 shows the average sample heating ΔT from Eq. (35) times the area of the illuminated spot $\pi(d/2)^2$ as a function of the photon energy E_γ for uranium samples of various thicknesses. In addition, Fig. 7 shows the average sample heating times the spot area as a function of sample thickness t for several materials at both $E_\gamma = 15 \text{ keV}$ and 50 keV .

A clear implication of this analysis is that for thin samples too much sample heating may be required, especially for small spot sizes, if the illumination is done rapidly compared to the time scale over which heat diffuses away from the illuminated region (see Sec. IV B 2 below). Optimizing the photon energy for the material of interest can help, although even for low-Z materials lower energies are of limited benefit since the absorption cross sections are so large. Mesoscale imaging is possible at hard x-ray energies because of the ability to transmit through a sufficiently thick sample, as well as due to the reduction in absorbed energy, which allows measurements to be made rapidly.

2. Temperature diffusion for multiple pulses

The preceding section attempted to estimate the temperature increase due to the energy deposited in the sample in a single pulse. What about the influence of a train of pulses? Does the temperature increase due to a single pulse have time to diffuse away before the next pulse arrives, thus allowing

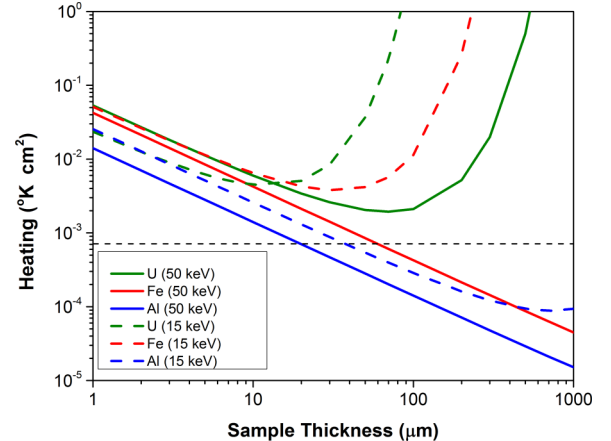


FIG. 7. (Color online) Average sample heating ΔT times the area of the illuminated spot $\pi(d/2)^2$ vs sample thickness t for three different elemental materials, using 50 keV photons [the vertical dotted line of Fig. (6)] (the solid curves) or 15 keV photons (the dashed curves). For reference, the dashed horizontal line corresponds to a 10 K temperature rise for a 100 μm spot.

the heating of the sample to effectively start anew with each pulse? Or, conversely, is there insufficient time for diffusion to take effect, so that the temperature increases due to subsequent pulses is cumulative?

The temperature distribution within a material illuminated by a given light source is governed by the heat equation,

$$\frac{\partial}{\partial \tau} T(\vec{r}, \tau) = \alpha \nabla^2 T(\vec{r}, \tau) + Q(\vec{r}, \tau), \quad (36)$$

$$T(\vec{r}, 0) = T_0.$$

Here $T(\vec{r}, \tau)$ is the temperature field, $\vec{r} = (x, y, z)$ is a position within the sample, τ is time (since t was already taken), α is the thermal diffusivity, ∇^2 is the Laplacian operator, T_0 is the initial temperature of the sample, and $Q(\vec{r}, \tau)$ is the position- and time-dependent rate at which the beam is changing the temperature within the material. For multiple diffractive images during a dynamic event, the heat source term can be considered a set of delta-functions in time of magnitude ΔT and separated by the time τ_b between subsequent x-ray pulses. It is straightforward to show that the time required for heat to diffuse away from a region of diameter d is of order d^2/α . For thermal diffusivities α typical of the materials of interest (see Table I) and spot sizes d large enough that the heating from a single pulse does not significantly perturb the sample, d^2/α is lies approximately in the range 0.1–1 milliseconds. Thus heating is cumulative on the microsecond time scales of the passage of a shock wave across a mesoscale region, but can diffuse away between subsequent pulses from a 50–120 Hz source.

V. SOME PROPOSED EXPERIMENTAL NUMBERS

In Table II we present numbers corresponding to three example mesoscale imaging experimental designs using iron (example 1) and uranium (examples 2 and 3). We have in all cases attempted to choose sample properties and experimental parameters which are workable and plausible, and which do not

TABLE II. Parameters for some example experiments.

Quantity	Description	Example 1	Example 2	Example 3
Z	Sample atomic number	26 (Fe)	92 (U)	92 (U)
λ	Source wavelength (\AA)	0.25	0.25	0.3
E_γ	Photon energy (keV)	50	50	41.3
d	Spot size (μm)	100	100	120
t	Sample thickness (μm)	500	100	200
iFOM	Imaging figure-of-merit	400	500	120
O_\perp	Transverse oversampling factor	2	2	2
p	Pixel size (μm)	12.5	12.5	12.5
$D = O_\perp \text{iFOM } p$	Detector size (cm)	1.0	1.25	0.3
L	Sample-detector distance (m)	100	100	100
$\phi_{\max} = \tan^{-1}(D/2L)$	Maximum scattering angle (rad)	5×10^{-5}	6.3×10^{-5}	1.5×10^{-5}
$\Delta x = L\lambda/D$	Transverse image resolution (nm)	250	200	1000
$\Delta z = 4\lambda L^2/D^2$	Longitudinal resolution (cm)	1.0	0.64	13
$\text{Fr} = d^2/\lambda L$	Fresnel number	4.0	4.0	5
$A_n = D^4/\lambda L^3$	Small angle number	4×10^{-4}	1×10^{-3}	3×10^{-6}
η_{QE}	Detector quantum efficiency	90%	90%	90%
P	Average photons per pixel	400	100	100
$1/\sqrt{P}$	Average-per-pixel noise-to-signal	5%	10%	10%
N_0	Required incident photons for imaging [Eq. (33)]	1.3×10^{10}	6.4×10^9	1.5×10^{10}
N_{1C}	Coherently-scattered photons for imaging [Eq. (31)]	2.8×10^8	1.1×10^8	6.4×10^6
N_{1C}/N_0	Fraction coherently scattered	2.3%	1.7%	0.04%
ΔT	Average temperature rise (K) [Eq. (35)]	3.4	27	23

yield too great a degree of heating in the sample. Nevertheless, there are a number of entries in Table II which hint at the inherent (though by no means insurmountable) difficulty of performing coherent diffraction imaging in dense materials. In particular, the large sample-to-detector distance $L = 100$ m imposes a stringent requirement on facility design. In addition, note that the longitudinal imaging resolution Δz is for all three examples significantly larger than the proposed sample thickness. This indicates that only two-dimensional CXDI is possible in these cases. The imaging data gathered would therefore consist of a projection of the sample's electron number density field $\rho(\vec{r})$ onto a plane perpendicular to the beam.

Figure 8 provides a simulated example—analogous to the examples in Fig. 3—of CXDI using a model sample and experimental geometry corresponding to example 2 in Table II. The contrast mechanism in this case is the variation in electron density near grain boundaries, and the resulting reconstructed image is a two-dimensional projection of this field. Grain boundary density contrast has previously been used in the

context of phase contrast imaging (PCI) in polycrystals (see, e.g. Kowalski *et al.* [35]). In addition, in a true dynamic, *in situ* imaging experiment, other contrast mechanisms, such as those associated with shock compression, would typically be present. The sample used in the analysis of Fig. 8 was modeled via a set of 100 randomly generated grain centers distributed through a 100 μm cube. The Voronoi tessellation associated with these centers was determined, and the corresponding electron density field was constructed by assigning a density equal to the average electron density of unshocked uranium to the central region of each grain, with a decrease in density near the grain boundaries peaking at a 10% decrease on the planes of the boundaries themselves. (The 10% figure is, to a certain extent, ad hoc, although it is in rough agreement with values obtained from unpublished molecular dynamics simulations of polycrystalline iron.)

As a final point, it is appropriate to include here some discussion of the question of coherence. In the preceding, we have neglected most of the details regarding the light source characteristics, and have instead assumed a perfect plane

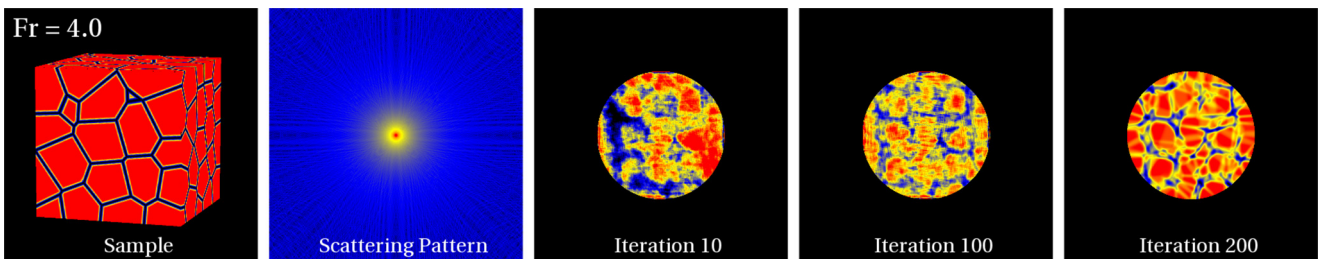


FIG. 8. (Color online) Simulated x-ray scattering and iterative phase retrieval using a 3D polycrystalline sample and experimental geometry analogous to example 2 in Table II. This calculation was done at $\text{Fr} = 4.0$.

wave source. In reality, x-ray free electron lasers (XFELs) such as those alluded to in Sec. I are not fully spatially coherent. The transverse coherency drops significantly as the normalized transverse emittance exceeds $\beta\gamma\lambda/\pi$ where γ and β are the usual relativistic factors. Vartanyants *et al.* [6] found the degree of transverse coherence to be 75% at the Linac Coherent Light Source (LCLS) at 8 keV. At shorter x-ray wavelengths achieving transverse coherence can be difficult. Increasing the electron energy and γ is not a solution as coherent synchrotron radiation can have deleterious effects at very high energies. Running at lower injection charge can increase the estimated coherence; for example, Schneidmiller and Yurkov [36] estimate the degree of coherence at the European XFEL to be approximately 90% at 10 keV, but 75% at 25 keV for the planned injection charge of that facility. A very-hard-x-ray FEL experimental facility such as the MaRIE facility [37] proposed by Los Alamos National Laboratory may require advanced design concepts [38] to achieve significant levels of transverse coherence.

Nevertheless, techniques are in use for ameliorating the effects of partial coherence. A full review of these techniques would be lengthy and well beyond the scope of this paper. Whitehead *et al.* [17] and the references therein describe a technique whereby the various modes present in the source wave incident upon the sample are themselves reconstructed as part of the IPR process. In addition the technique of *ptychography*, in which the phase/intensity profile of a source is calculated in the absence of a sample prior to the imaging experiment, is in wide use (see, e.g., Kewish *et al.* [39] and Schropp *et al.* [40]).

VI. CONCLUSIONS

The detailed study of dynamic material properties at the mesoscale, i.e., three-dimensional samples comprising tens to hundreds of grains of material, requires dynamic imaging, which could be possible with coherent diffraction imaging using highly penetrating photons. The combination of large spot sizes and high energy photons leads to large Fresnel number optical systems that do not allow for the Fraunhofer far-field limit approximations. This paper showed that diffractive imaging using hard x rays is possible at large Fresnel numbers, and extends the Fresnel regime analysis to coherent x-ray diffraction imaging and phase retrieval algorithms. From the resulting analysis the optimal photon energy can be chosen for a given per-pixel signal-to-noise, and the maximum photon bandwidth can be calculated. An important aspect in experimental design is maximizing the coherently scattered photons relative to the absorbed photons since the absorbed photons can cause heating easily high enough to melt or vaporize the sample from a single pulse making multiple-pulse imaging all but impossible. Finally, we have applied the analytical techniques developed in this paper to three hypothetical experiments involving samples of either iron or uranium, to show that while the imaging of high-density, relatively thick samples presents experimental challenges, those challenges can be overcome with proper experiment design.

APPENDIX: LIST OF SYMBOLS

Light Source Parameters	
Symbol	Description
d	Source spot diameter or FWHM of intensity profile
λ	Source wavelength
E_γ	Source photon energy ($=hc/\lambda$)
\vec{k}_i	Source wave vector
k	Source wave number ($= \vec{k}_i $)
$\hat{\varepsilon}$	Polarization vector of the source
N_0	Total number of photons in a single pulse of the source
τ_b	Time between subsequent light source pulses

Sample Parameters	
Symbol	Description
t	Sample thickness in beam direction (usually the z direction)
$N_U(t)$	Number of unscattered photons which emerge from a sample thickness t
$N_{1C}(t)$	Number of photons which emerge from a sample thickness t that have undergone a single coherent scattering event as their sole interaction

Detector Parameters	
Symbol	Description
L	Sample-detector distance
ϕ	Maximum scattering angle subtended by the detector [$=\tan^{-1}(D/2L) = 2\theta_{\max}$]
D	Width/height of the detector
p	Width/height of the detector pixels
N_p	Number of pixels in each direction on the detector ($=D/p$)
P	Number of photons captured by an average detector pixel
η_{QE}	Quantum efficiency of the detector

Imaging Parameters	
Symbol	Description
Δx	Transverse (perpendicular to beam direction) resolution of sample image
Δz	Longitudinal (parallel to beam direction) resolution of sample image
O_\perp	Oversampling ratio in each of the two transverse directions
O_\parallel	Oversampling ratio in the longitudinal direction
iFOM	Imaging figure-of-merit in the transverse direction ($=dD/\lambda L \approx D/O_\perp p$)

Miscellaneous	
Symbol	Description
Fr	Fresnel number ($=d^2/\lambda L$)
An	Small-angle number ($=D^4/\lambda L^3$)
τ	Time (since t was already taken)
$\hat{e}_x, \hat{e}_y, \hat{e}_z$	Unit vectors in the x , y , and z coordinate directions

- [1] Basic Energy Science Advisory Panel, New Science for a Secure and Sustainable Energy Future, Tech. Rep., Basic Energy Sciences, U.S. Department of Energy, 2008.
- [2] J. Sarrao (ed.), Decadal Challenges for Predicting and Controlling Materials Performance in Extremes, Los Alamos National Laboratory, 2009.
- [3] G. Crabtree and J. Sarrao, From Quanta to the Continuum: Opportunities for Mesoscale Science, a Report from the Basic Energy Sciences Advisory Committee, 2012.
- [4] H. N. Chapman and K. A. Nugent, *Nat. Photonics* **4**, 833 (2010).
- [5] B. Abbey, *JOM* **65**, 1183 (2013).
- [6] I. A. Vartanyants, A. Singer, A. P. Mancuso, O. M. Yefanov, A. Sakdinawat, Y. Liu, E. Bang, G. J. Williams, G. Cadenazzi, B. Abbey, H. Sinn, D. Attwood, K. A. Nugent, E. Weckert, T. Wang, D. Zhu, B. Wu, C. Graves, A. Scherz, J. J. Turner, W. F. Schlotter, M. Messerschmidt, J. Lüning, Y. Acremann, P. Heimann, D. C. Mancini, V. Joshi, J. Krzywinski, R. Soufli, M. Fernandez-Perea, S. Hau-Riege, A. G. Peele, Y. Feng, O. Krupin, S. Moeller, and W. Wurth, *Phys. Rev. Lett.* **107**, 144801 (2011).
- [7] D. Sayre, *Acta Crystallogr.* **5**, 843 (1952).
- [8] J. W. Miao, P. Charalambous, J. Kirz, and D. Sayre, *Nature (London)* **400**, 342 (1999).
- [9] G. J. Williams, M. A. Pfeifer, I. A. Vartanyants, and I. K. Robinson, *Phys. Rev. Lett.* **90**, 175501 (2003).
- [10] I. Robinson and I. Harder, *Nat. Mater.* **8**, 291 (2009).
- [11] C. Song, H. Jiang, A. Mancuso, B. Amirkian, L. Peng, R. Sun, S. S. Shah, Z. H. Zhou, T. Ishikawa, and J. Miao, *Phys. Rev. Lett.* **101**, 158101 (2008).
- [12] M. M. Seibert, T. Ekeberg, F. R. N. C. Maia, M. Svenda *et al.*, *Nature (London)* **470**, 78 (2011).
- [13] J. Nelson, X. Huang, J. Steinbrener, D. Shapiro, J. Kirz, S. Marchesini, A. M. Neiman, J. J. Turner, and C. Jacobsen, *Proc. Natl. Acad. Sci. USA* **107**, 7235 (2010).
- [14] D. Shapiro, P. Thibault, T. Beetz, V. Elser, M. Howells, C. Jacobsen, J. Kirz, E. Lima, H. Miao, A. M. Neiman *et al.*, *Proc. Natl. Acad. Sci. USA* **102**, 15343 (2005).
- [15] A. Barty, J. Küpper, and H. N. Chapman, *Annu. Rev. Phys. Chem.* **64**, 415 (2013).
- [16] B. Abbey, G. J. Williams, M. A. Pfeifer, J. N. Clark, C. T. Putkunz, A. Torrance, I. McNulty, T. M. Levin, A. G. Peele, and K. A. Nugent, *Appl. Phys. Lett.* **93**, 214101 (2008).
- [17] L. W. Whitehead, G. J. Williams, H. M. Quiney, D. J. Vine, R. A. Dilanian, S. Flewett, K. A. Nugent, A. G. Peele, E. Balaur, and I. McNulty, *Phys. Rev. Lett.* **103**, 243902 (2009).
- [18] G. J. Williams, H. M. Quiney, B. B. Dhal, C. Q. Tran, K. A. Nugent, A. G. Peele, D. Paterson, and M. D. de Jonge, *Phys. Rev. Lett.* **97**, 025506 (2006).
- [19] B. Warren, *X-Ray Diffraction* (Dover Publications, Mineola, NY, 1990).
- [20] J. D. Jackson, *Classical Electrodynamics*, 3rd ed. (John Wiley & Sons, Inc., New York, 1999).
- [21] H. M. Quiney, K. A. Nugent, and A. G. Peele, *Opt. Lett.* **30**, 1638 (2005).
- [22] W. T. Cathey, *Optical Information Processing and Holography* (John Wiley & Sons, Inc., New York, 1974).
- [23] X.-H. Xiao and Q. Shen, *Phys. Rev. B* **72**, 033103 (2005).
- [24] H. Römer, *Theoretical Optics: An Introduction* (Wiley-VCH Verlag GmbH & Co. KGaA, Weinheim, 2005).
- [25] K. S. Raines, S. Salha, R. L. Sandberg, H. Jiang, J. A. Rodriguez, B. P. Fahimian, H. C. Kapteyn, J. Du, and J. Miao, *Nature (London)* **463**, 214 (2010).
- [26] M. D. Seiberg, D. E. Adams, E. L. Townsend, D. A. Raymondson, W. F. Schlotter, Y. Liu, C. S. Menoni, L. Rong, C.-C. Chen, J. Miao *et al.*, *Opt. Express* **19**, 22470 (2011).
- [27] C.-C. Chen, H. Jiang, L. Rong, S. Salha, R. Xu, T. G. Mason, and J. Miao, *Phys. Rev. B* **84**, 224104 (2011).
- [28] J. R. Fienup, *J. Opt. Soc. Am. A* **4**, 118 (1987).
- [29] J. Miao, D. Sayre, and H. N. Chapman, *J. Opt. Soc. Am. A* **15**, 1662 (1998).
- [30] J. Miao, T. Ishikawa, E. H. Anderson, and K. O. Hodgson, *Phys. Rev. B* **67**, 174104 (2003).
- [31] S. Marchesini, *Rev. Sci. Instrum.* **78**, 011301 (2007).
- [32] B. Liu and N. C. Gallagher, *Appl. Opt.* **13**, 2470 (1974).
- [33] M. Berger, J. Hubbell, S. Seltzer, J. Chang, J. Coursey, R. Sukumar, D. Zucker, and K. Olsen, XCOM: Photon Cross Sections Database, Ver. 1.5, <http://physics.nist.gov/xcom>, National Institute of Science and Technology, Gaithersburg, MD, 1990.
- [34] D. R. Lide (ed.), *CRC Handbook of Chemistry and Physics*, 75th ed. (CRC Press, Boca Raton, FL, 1994).
- [35] G. Kowalski, M. Moore, and S. Nailer, *J. Phys. D: Appl. Phys.* **32**, A166 (1999).
- [36] E. A. Schneidmiller and M. V. Yurkov, Photon Beam Properties at the European XFEL, Tech. Rep. XFEL.EU TR-2011-006, European X-Ray Free-Electron Laser Facility GmbH, Hamburg, Germany, 2011.
- [37] R. L. Sheffield and B. E. Carlsten, Pre-Conceptual Design Requirements for the MaRIE Facility at LANL and the Resulting X-Ray Free Electron Laser Baseline Design, Tech. Rep., 2011, dataset: DUSA.
- [38] B. E. Carlsten, C. W. Barnes, K. A. Bishopberger, L. D. Duffy, C. E. Heath, Q. R. Marksteiner, D. C. Nguyen, S. J. Russell, R. D. Ryne, R. L. Sheffield, E. I. Simakov, and N. A. Yampolsky, MaRIE X-Ray Free-Electron Laser Pre-Conceptual Design, Tech. Rep., 2011, dataset: DUSA.
- [39] C. M. Kewish, M. Guizar-Sicairos, C. Liu, J. Qian, B. Shi, C. Benson, A. M. Khounsary, J. Vila-Comamala, O. Bunk, J. R. Fienup, A. T. Macrander, and L. Assoufid, *Opt. Express* **18**, 23420 (2010).
- [40] A. Schropp, R. Hoppe, V. Meier, J. Patommel, F. Seiboth, H. Lee, B. Nagler, E. C. Galtier, B. Arnold, U. Zastrau, J. B. Hastings, D. Nilsson, F. Uhlén, U. Vogt, H. M. Hertz, and C. G. Schroer, *Sci. Rep.* **3**, 1633 (2013).